Geophys. Res. **93**, 14881 (1988).
13. G. H. Pettengill, P. G. Ford, S. Nozette, *Science* **217**, 640 (1982); P. G. Ford and G. H. Pettengill, *ibid.*, p. 220.
14. V. L. Barsukov *et al.*, *J. Geophys. Res.* **91**, D378 (1986); A. T. Basilevsky *et al.*, *ibid.*, p. D399; B. A. Ivanov *et al.*, *ibid.*, p. D413.
15. Yu. N. Alexandrov *et al.*, *Science* **231**, 1271 (1986).
16. R. M. Goldstein *et al.*, *Icarus* **36**, 334 (1978); R. F. Jurgens, R. M. Goldstein, H. R. Rumsey, R. R. Green, *J. Geophys. Res.*, **85**, 8282 (1980); R. F. Jurgens *et al.*, *Geophys. Res. Lett.* **15**, 577 (1988).
17. P. G. Ford and D. A. Senske, *Geophys. Res. Lett.* **17**, 1361 (1990).
18. Six elevated regions observed by Pioneer Venus at a wavelength of 17 cm (Ovda Regio, Thetis Regio, Maat Mons, Ozza Mons, Theia Mons, and Rhea Mons) have an average surface reflection coefficient of 0.39 ± 0.03 and an average surface emissivity of 0.61 ± 0.11, where the indicated variation is 1 SD of the reported values in tables 2 and 3 of (*12*). Also see R. Arvidson, Ed., *Pre-Magellan Radar and Gravity Data* (*USA NASA JPL MG-1001*, Planetary Data System, NASA, Washington, DC, 1990).
19. The Hagfors law is from T. Hagfors, *J. Geophys. Res.* **69**, 3779 (1964). The close relation between the physical-geometric optics formulation and quasi-specular scatter, which forms the basis for much of the geological interpretation of planetary radar data, is given in T. Hagfors, *J. Geophys. Res.* **71**, 379 (1966). The approximate relation between rms surface slope and the Hagfors parameter C is derived in "Radar Studies of the Moon" (*Final Rep.*, vol. 1, Lincoln Laboratory, Lexington, MA, 1967). Generally for models of natural surfaces, inferred rms slopes refer to a smoothed version of the actual surface, that is, to the long-wavelength portion of the surface height spectrum. The "filtering" process by which the effective portion of the spectrum is selected is not well-understood. Also, see (*20*).
20. The horizontal scale to which an rms slope measurement applies depends on several factors, including the height spectrum of the surface [G. L. Tyler, *Radio Sci.* **11**, 83 (1976)]. Empirical comparison of radar results with photoclinometric and photogrammetric estimates of lunar slopes suggests that the radar rms slope is an effective value representing an average over scales from a few to a few hundred wavelengths (*9*), hence the range quoted for Magellan.
21. Use of the spacecraft high-gain antenna for radiometry effectively limits the range of emission angles sensed to the antenna beamwidth, which is slightly over 2°, one way, full width at the half-power response points. Observations represent beam-weighted averages about the mean angle. The angle of the beam axis with respect to the surface varies, depending on the programming of the SAR observations. For the primary mission, a minimum emission angle of about 17° obtains near the north pole, whereas the value near periapsis at 10°N is 47°. The situation is slightly different for the SAR as range processing of the radar echoes provides the ability to discriminate echoes as a function of angle independently of the antenna characteristics. In principle it is possible to measure the variation of the echo strength with scattering angle, and hence to estimate the slope of the scattering law across the SAR swath as well as the average value. Whether this can be achieved in a meaningful way in practice, given changes in the surface characteristics evident in many of the SAR images, remains to be seen. In any event the scattering law is expected to be well constrained by the measurements about the nadir plus at least one constraining value at moderate values of the angle of incidence (compare Figs. 1 and 2).
22. The bandwidth for radiometry is 10 MHz, detected and accumulated for 50 ms, yielding a time-bandwidth product of 5×10^5. The radiometry signal is obtained alternately from the high-gain antenna and from a comparison load at known temperature. In this way variations in receiver gain can be compensated relatively accurately over short time intervals to a precision of about 2 K; the absolute accuracy is about 15 K.
23. The half-power half-beamwidth of the altimetry antenna is about 5° in the direction of spacecraft motion and about 15° at right angles to the orbit plane. The useful range of incidence angles sensed depends on several factors, some of which change with position along the orbital track. At the highest altitudes, over the polar regions, altimeter echoes are aliased in the frequency domain at a folding point corresponding to about 7° angle of incidence, and in the time domain at a folding point corresponding to about 6° angle of incidence. Near periapsis, these values are about 3.3° and 15° angle of incidence, respectively. Superposition of echoes from different pulses, or range aliasing, is unavoidable, but in some circumstances the antenna pattern can be used to ensure that echoes from distant parts of the surface will be weak. In others, the scattering function itself guarantees that near-nadir echoes dominate.
24. Calibration of the SAR backscatter is based on the radar equation, laboratory measurements of the SAR system parameters, and tests for internal consistency of the data.
25. L. Tsang, J. A. Kong, R. T. Shin, *Theory of Microwave Remote Sensing*, (Wiley, New York, 1985). In obtaining the value of emissivity from the data, it is assumed that the surface is in thermal equilibrium with the atmosphere (*4*).
26. G. S. Downs, R. M. Goldstein, R. R. Green, G. A. Morris, P. E. Reichley, *Icarus* **18**, 8 (1973); G. H. Pettengill, I. I. Shapiro, A. E. E. Rogers, *ibid.*, p. 22.
27. G. L. Tyler and D. H. H. Ingalls, *J. Geophys. Res.* **76**, 4775 (1971).
28. M. N. Parker, thesis, Stanford University, Palo Alto, CA (1973); B. J. Lipa, and G. L. Tyler, *Icarus* **28**, 301 (1976).
29. M. N. Parker and G. L. Tyler, *Radio Sci.* **8**, 177 (1973).
30. R. A. Simpson and G. L. Tyler, *IEEE Trans.* **AP-30**, 438 (1982).
31. R. A. Simpson, G. L. Tyler, G. G. Schaber, *J. Geophys. Res.* **89**, 10385 (1984).
32. Full analysis requires calibration of both the SAR and altimeter data and estimation of scattering efficiency at angles not observed by either (Fig. 2).
33. Pioneer Venus resolution of radiometric observations varied from approximately 90 km at periapsis to more than 1000 km at the highest operating altitudes. The best emissivity measurements from Earth have resolutions of a few hundred kilometers.
34. The highest reported point lies at 64°N, 2°E, [G. H. Pettengill *et al.*, *J. Geophys. Res.* **85**, 8261 (1980)]. Also, see (*15*).
35. Horned features are postulated to result from wind-carried ejecta associated with impact processes [R. E. Arvidson *et al.*, *Science* **252**, 270 (1991)].
36. J. W. Head *et al.*, *Science* **252**, 276 (1991); D. B. Campbell *et al.*, *ibid.* **246**, 373 (1989).
37. Changes in surface composition that enhances horizontally polarized radar backscatter do so for all incidence angles, whereas enhancements at high incidence angles resulting from increased roughness will be offset by a decrease in radar backscatter near the nadir. Comparison of $\sigma_0(\theta_i)$ measurements from the SAR and altimeter, in conjunction with emissivity measurement, permits separation of roughness and composition effects.
38. Pettengill *et al.* (*12*) report a lowlands average radar reflectivity of 0.14, corresponding to an effective dielectric constant of 5.0; values for reflectivity in highlands regions vary from more than 0.4 (dielectric constant >20) for Maxwell Montes to typical values in the range of 0.35 to 0.40 (dielectric constant 15 to 20) for the six features named in (*18*). We quote values for dielectric constant calculated for a lossless material with relative permeability of unity for convenience only. There is no intent to imply that the actual material is so ideal.
39. At 6055 km the atmospheric temperature and pressure are 712.4 K and 76.01 bars, respectively; at the reference radius of 6051 km they are 743.0 K and 98.12 bars [A. J. Kliore, V. I. Moroz, G. M. Kesting, *Adv. Space Res.* **5**, 11 (1985)].
40. This work has been made possible by the dedicated efforts of many people associated with the Magellan Project at the Jet Propulsion Laboratory and at the authors' home institutions. We especially thank W. T. K. Johnson and P. Graf. We also thank F. Liu, J. Quigley, and M. Maurer.

8 January 1991; accepted 14 March 1991

Magellan: Initial Analysis of Venus Surface Modification

R. E. ARVIDSON, V. R. BAKER, C. ELACHI, R. S. SAUNDERS, J. A. WOOD

Initial Magellan observations reveal a planet with high dielectric constant materials exposed preferentially in elevated regions with high slopes, ejecta deposits extending up to 1000 kilometers to the west of several impact craters, windblown deposits and features in areas where there are both obstacles and a source of particulate material, and evidence for slow, steady degradation by atmosphere-surface interactions and mass movements.

RADAR OBSERVATIONS OF VENUS made by the Earth-based Arecibo and Goldstone facilities and by the Venera 15–16 spacecraft demonstrated that volcanic and tectonic landforms dominate the surface of that planet (*1*). However, the nature and extent of landform modification by such processes as chemical and mechanical weathering, eolian (that is, wind-related) processes, and mass wasting have remained unclear. The reason is that the spatial resolution of these observations is too coarse to resolve the relatively fine-scale features produced by such processes. For example, simulations with the use of Seasat radar images of Earth showed that the Gran Desierto dunes, the largest dune field in North America, would not be discernible at the resolu-

R. E. Arvidson, McDonnell Center for the Space Sciences, Department of Earth and Planetary Sciences, Washington University, St. Louis, MO 63130.
V. R. Baker, Department of Geosciences, University of Arizona, Tucson, AZ 85721.
C. Elachi and R. S. Saunders, Jet Propulsion Laboratory, 4800 Oak Grove Drive, Pasadena, CA 91109.
J. A. Wood, Smithsonian Astrophysical Observatory, 60 Garden Street, Cambridge, MA 02139.

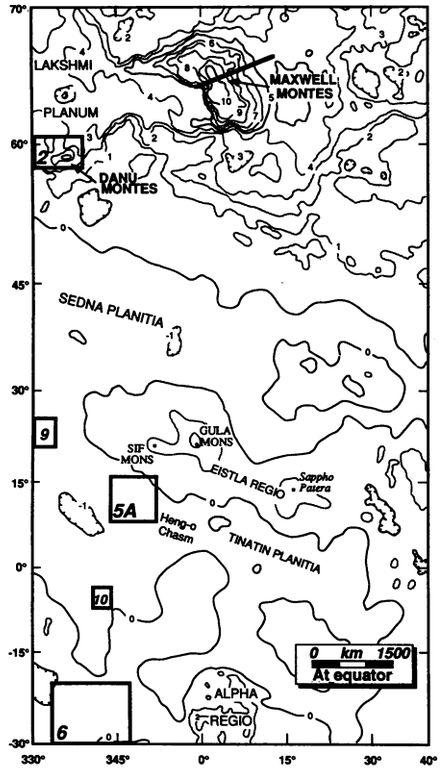

Fig. 1. Location map showing regions discussed in this paper. Contours are derived from Pioneer-Venus data and are elevations in kilometers relative to the mean radius of Venus. Southwest-northeast line across Maxwell Montes delineates location of profile data shown in Fig. 3. Boxes show locations of selected figures. [Mercator projection]

tion of the data available from Arecibo, Goldstone, or Venera observations (*2*). The Magellan mission has now provided images of the surface at high enough spatial resolution to be able to see the fine-scale features diagnostic of weathering, erosion, and deposition (*3*). In this report, we analyze initial Magellan observations that pertain to understanding the nature, rate, and history of these surficial processes. We focus on radar imaging, although we also discuss results from radiometry and altimetry observations.

Pre-Magellan observations did provide some first-order information on the average rate of modification of the surface and the nature of surface materials. On the basis of the degree of preservation of crater ejecta, the extent of resurfacing by mechanical and chemical weathering, erosion, and burial (by wind and mass movements) was estimated to be insignificant averaged over the several hundred million year surface age and limited to reworking of the top few meters of surface material (*4*). On the other hand, laboratory experiments on the kinetics of weathering (*5*) and analyses of the ability of the dense venusian atmosphere to move sand and dust (*6*) suggested that weathering and erosion have occurred at much higher rates. Analyses of Pioneer-Venus radar observations suggested that surfaces at high elevations expose minerals with high dielectric constants, for example: pyrite, magnetite, or ilmenite (7). The Pioneer-Venus data analyses also showed that the average Fresnel reflectivity (at 17-cm wavelength) for the planet is about 0.14. This value implies that bedrock or highly packed debris dominates the surface and that fine-grained soil cover is restricted to less than tens of centimeters in thickness. The tesserae, regions that have been subjected to complex tectonic deformation, were found to be exceptions. For the tesserae, Fresnel reflectivities were found to be consistent with the presence of thick soil deposits (*7, 8*).

Analysis of Magellan altimetric data (*9*) generally confirm the Fresnel reflectivity and roughness estimates derived from Pioneer-Venus observations. In addition, emissivity-values derived from the radiometry mode of the Magellan Radar System (*9*) also are consistent with Pioneer-Venus results. Low emissivities were observed by Magellan on several topographically high regions (Fig. 1): Maxwell Montes, Danu Montes, Gula Mons, and Sif Mons. Complex relations are observed among radar backscatter cross section, elevation, and emissivity in these areas. For example, emissivity decreases only over a part of the topographically rough terrain making up Danu Montes (*10*) (Fig. 2). Moreover, the occurrence of low-emissivity surfaces is not simply related to elevation because the low-emissivity region is displaced northwestward relative to the peak elevation for Danu Montes. In addition, not all surface materials at high elevations have low emissivities. For example, the flanks of Maxwell Montes exhibit the lowest emissivities, whereas material at the summit has a higher emissivity (Fig. 3). For Maxwell Montes, areas of low emissivity correlate better with large-scale slope than with elevation.

A plausible explanation for the patterns

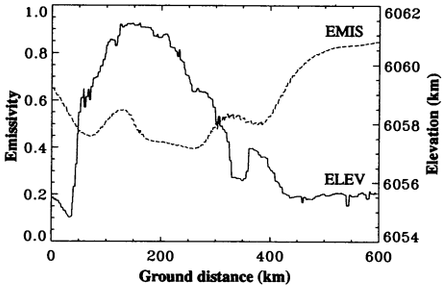

Fig. 3. Profiles of emissivity (EMIS) and elevation (ELEV) across Maxwell Montes. Maxwell is the high area on the left of the profile. Left end of profile is located at 64.7° latitude, 359° longitude; right end is located at 67.3° latitude, 13.5° longitude. Emissivities are lowest in those parts of Maxwell Montes that have steepest regional slopes.

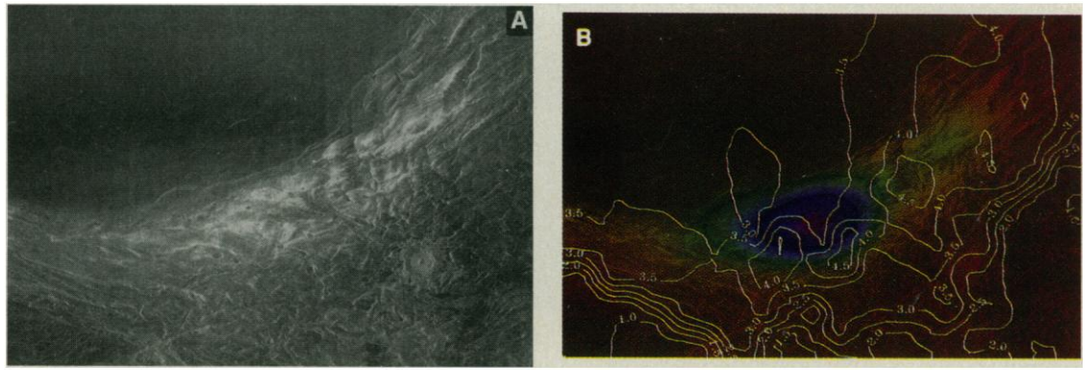

Fig. 2. (**A**) Radar mosaic covering Danu Montes, part of Lakshmi Planum to the north, and terrain to the south. Danu Montes is the rugged terrain with high cross sections. Note the impact crater with a central peak and flat floor located in the southeastern part of the mosaic. Part of F-MIDR 60N334, covering an area approximately 440 km wide. Incidence angle is approximately 28°. Center latitude is 59.2°; center longitude is 334.9°. This and subsequent figures are based on Magellan data shown using sinusoidal equal area projections. All Magellan radar look directions are from the west. (**B**) Overlay of (A) with color-coded emissivity values. Cool colors (purple) correspond to an emissivity of 0.76 and warm (red) colors to a value of 0.88. Emissivity is lowest in Danu Montes. This low emissivity area is not the topographically highest terrain in the region. Contours are elevations in kilometers above 6051-km radius.

seen in the altimetric data is that unweathered surface materials contain high-dielectric-constant minerals that are unstable in contact with the planet's atmosphere. Over most of the planetary surface, the material has reacted with the atmosphere to form products with low dielectric constants, but chemically weathered material may be eroding from steep slopes rapidly enough so that fresh rock that contains the critical material is constantly exposed. Enhanced mass wasting associated with steep local slopes, coupled with high winds induced by regional-scale slopes, may cause the increased erosion. Slump blocks and landslides have been observed in Magellan images of mountainous terrains, and Saunders *et al.* (*11*) predicted that highest winds (several meters per second at the surface) occur in areas with steepest regional-scale slopes. Other low-emissivity areas on Venus, notably in the lowlands west of Atalanta Planitia (*7*), however, are neither high nor sloping. Thus, this simple hypothesis offers only a partial explanation of the observations, and a more complete model must await acquisition, reduction, and analysis of the full Magellan data set.

Another set of regional-scale features evident in the Magellan data are prominent low-emissivity streaks located within 30° of the equator (Fig. 4). The streaks define parabolic shapes to first order, and have varying distances from foci to vertices. An impact crater is located close to the focus of each paraboloidal streak. The vertices are all on eastern edges of the paraboloids and the axes are parallel with lines of latitude. These features have east-west dimensions between 500 and 1000 km.

The paraboloidal streaks typically have both low radar backscatter cross sections and emissivities. For example, the southern arm of the streak located to the southwest of Sif Mons (Fig. 5) is particularly well developed and has emissivity values that range from about 0.77 to 0.80, as compared to values between 0.83 to 0.86 for the immediate surroundings. Also, the backscatter cross section for the southern arm is approximately 3 to 5 dB lower than that in the surrounding areas. The low radar cross sections and emissivities imply that the streak material is smooth relative to its surroundings. Similar differences are observed for basaltic lava flows of different ages on Earth. For example, in the Cima Volcanic Field, Mojave Desert, southern California, the cross sections for horizontally polarized (transmitted and received) radar images in C and L bands observed for flows emplaced 180,000 years ago is 3 to 5 dB higher than for flows emplaced 850,000 years ago (*12*). Older flows have been smoothed by mass wasting and deposition of eolian dust, silt, and sand.

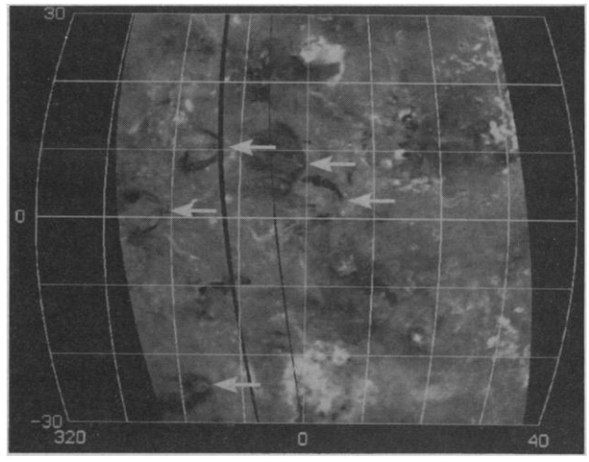

Fig. 4. Gray-tone image of emissivity for regions within 30° of the equator. Emissivities below 0.79 are set to black; values above 0.89 are set to white. Arrows delineate the eastern edges of low-emissivity, paraboloidal streaks that open toward the west and that have axes parallel to latitudes. Each is associated with an impact crater located near the eastern side of the respective streak.

Further evidence for the smooth nature of streak surfaces comes from combined analyses of Magellan altimetric and SAR data. The average Fresnel reflectivity estimated from altimetric data for the paraboloidal streak shown in Fig. 5 is 0.15, as opposed to a value of 0.13 for the surrounding area. Correcting for the diffuse-scale roughness component in the Fresnel reflectivity, as done by Pettengill *et al.* (*7*), lowers the value for the paraboloidal streak to about 0.14. The similarity in the reflectivity estimates within and outside of the streak implies that most of the variation in emissivity is a result of roughness at the scale of the radar wavelength. That is, the streak is smoother than the surrounding region at about a 12.6-cm length scale. Finally, the quasi-specular-scale (>12.6 cm) root-mean-square (rms) slope values estimated from altimetric data (*9*) are higher in this paraboloidal streak than in the surrounding region (5° versus 2.5°).

A complex paraboloidal streak associated with the 38-km diameter crater Carson provides additional information on paraboloidal streak characteristics (Fig. 6). For example, several ~10 km long streaks extend from domes located within the eastern segment of the paraboloidal streak (Fig. 7). We believe that these small streaks are the result of perturbation of wind flow by the domes. Such features have been produced in wind tunnels, are found on Earth and Mars, and are evident in SIR-A and Seasat radar images of Earth (*6, 13*). Vortices shed by wind flowing over obstacles cause erosion directly downwind, and deposition occurs at the edges of the erosive zone. Deposition is related to upward motions of the vortices (*13*). The north-northwest trending streak to the northeast of Carson has a backscatter cross section that is approximately 9 dB higher than that of the surroundings. Most likely, ejecta material has been eroded down-

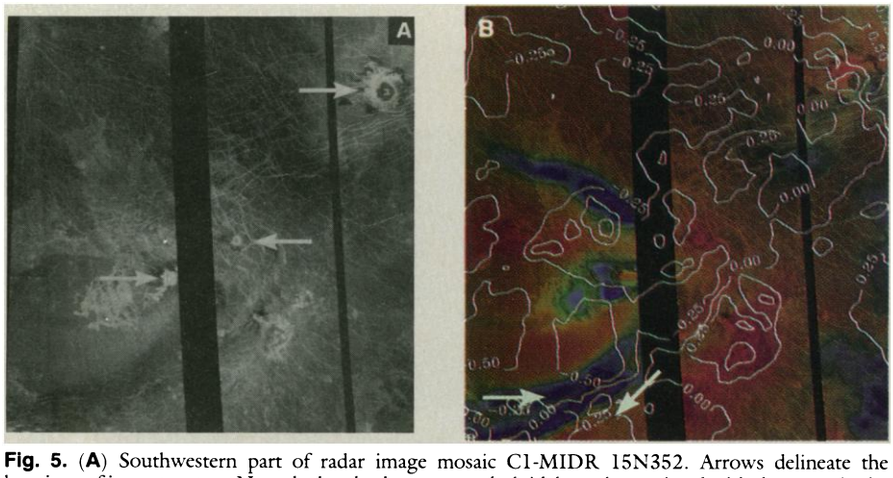

Fig. 5. (**A**) Southwestern part of radar image mosaic C1-MIDR 15N352. Arrows delineate the locations of impact craters. Note the low backscatter paraboloidal streak associated with the crater in the lower left center. Incidence angle is approximately 45°. Center latitude is 11.7°; center longitude is 347.3°; the frame covers an area approximately 870 km wide. (**B**) Overlay of (A) with color-coded emissivity values. Blue corresponds to an emissivity of 0.77 and red to 0.90. Contours are elevations relative to a radius of 6051 km, in 0.25-km intervals. Arrows denote areas for which emissivity and backscatter properties were extracted, as discussed in text.

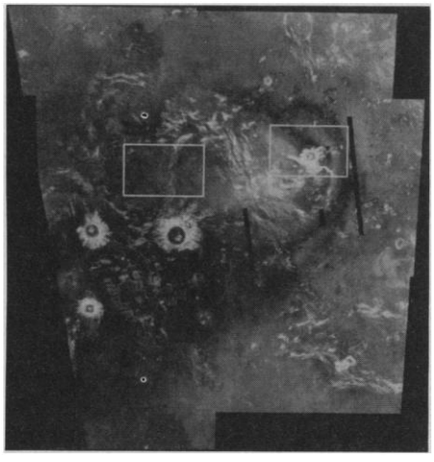

Fig. 6. Regional-scale radar mosaic covering a group of four craters informally called the "crater farm." Carson is the easternmost crater with the complex paraboloidal streak. Elevation contours with 0.25-km intervals are overlain. Boxes show locations of enlargements shown in Figs. 7 and 8. F-MIDRs 20S337, 20S344, 25S339, 25S345, and 30S338. Incidence angle is approximately 35°. Center latitude is −26.3°; center longitude is 341°. Mosaic is approximately 1250 km wide.

ward of this dome to produce this high backscatter dome-related streak. To the north of the region covered by Fig. 7 there are also a number of other dome-related streaks with high backscatter cores and low backscatter perimeters. These dome-related streaks appear to form because the paraboloidal streak provides a supply of fine particulate material, the domes form suitable local topographic obstacles, and because winds exceed the threshold required to erode material.

Winds above the first scale height on Venus are strongly zonal and retrograde (that is, westward); velocities are about 100 m/s at a height of approximately 60 to 70 km (*14*). In contrast, winds close to the surface have velocities of approximately 1 m/s (*15*), and the flow direction is uncertain, although theoretical models imply that there should be meridional flow driven by Hadley cell circulation (*14*) and zonal flow forced by differential solar heating related to the longitude of local noon (*16*). The large distances covered by the paraboloidal streaks suggest that the surface has interacted with the high-velocity retrograde winds. Furthermore, the paraboloidal shape provides an important constraint on the mechanism of emplacement. Initial calculations suggest that material ejected from cratering events toward the west becomes widely dispersed by retrograde winds, whereas material ejected toward the east would be deflected back toward the crater. Ejecta moving to the north and south would be systematically deflected westward. The overall depositional pattern outlines a paraboloidal shape.

The impact model nicely accounts for the geometric patterns associated with paraboloidal streaks. However, the volume of material required poses a potential problem. Each paraboloidal streak covers roughly 100 times the area of the associated crater. If the deposits are tens of centimeters thick, then approximately 10% of the crater ejecta would need to be thrown aloft and carried westward by retrograde winds. It is not clear that enough fine debris would be produced to be carried up to 1000 km to the west of the craters. An alternate explanation is that the paraboloidal streaks are produced by long-term weathering and eolian redistribution of ejecta by surface winds with a strong westward component. However, the dome-related streak directions shown in Fig. 7 suggest that surface winds are more complex than simple westward flow. Some streaks to the east of Carson trend north to north-northwest and follow topographic contours. A few trend west-northwest and north-northeast and are perpendicular to elevation contours. These relations imply that regional-scale topography has exerted a complex control on dome-related streak orientations. Furthermore, no east-west trending, dome-related streaks are found in the tails of the paraboloidal streaks associated with Carson or with other craters.

Whatever the detailed origin of the paraboloidal streaks, it is important that only seven to eight craters have these paraboloidal features. We postulate that these are the youngest craters because they still retain full ejecta deposits, including paraboloidal streaks. The overall crater retention age, based on the 135 craters inventoried in the region covered by Magellan, is approximately 400 Ma (*17, 18*). The youngest seven or eight craters must have formed during approximately the past 20 million years. If we assume that the paraboloidal streaks are ejecta deposits that are 1 m thick, then it follows that this amount of material must be redistributed over about 20 million years. This analysis implies that the average eolian redistribution rate of these deposits has been approximately 5×10^{-2} μm/yr. This rate is more than an order of magnitude less than the rate inferred for volcanic and tectonic processes that are thought to dominate crater removal (*17, 18*). The paraboloidal streaks also have potential use as time stratigraphic markers. For example, the western half of the volcano Gula Mons is covered by a paraboloidal streak associated with a crater just to the east of the volcano. A careful search was made to find lava flows that cover paraboloidal material. Such flows would have to be geologically quite young. None were found; thus, the flows on Gula all predate deposition of the streak material.

A speckle-like pattern may indicate the presence of a dune field within and adjacent to a complex ejecta flow (*19*) that extends northward from the 65-km-diameter crater located in the crater farm (Fig. 6). Terrestrial dunes imaged by radar have the same speckle-like appearance, where the speckle is associated with returns from dune faces tilt-

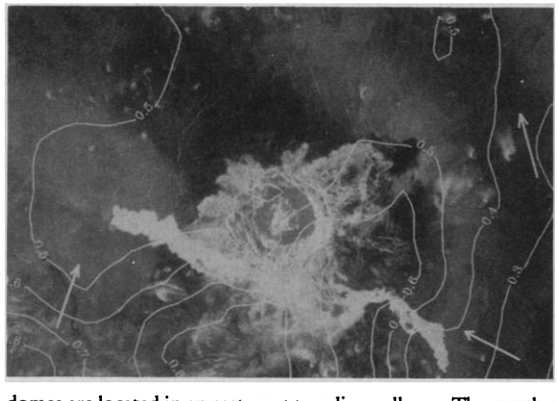

Fig. 7 (left). Part of radar mosaic shown in Fig. 6, centered on the crater Carson, with elevation contours overlain. Arrows denote directions of wind streaks associated with domical hills. Frame width is 218 km.

Fig. 8 (right). Part of radar mosaic shown in Fig. 6, centered on the crater ejecta flow extending to north of a 65-km-diameter crater in the crater farm area. Elevation contours are overlain. Streaks associated with domes are located in an east-west trending valley on the eastern edge of the mosaic and fan out in the flat terrain to the west. The north-south trending region of speckled return in the middle of the figure is suggestive of returns from a dune field. Frame width is 220 km.

ed toward the radar (*20*). The lateral dimensions and appearance of this candidate dune field are similar to those of the terrestrial Gran Desierto field as imaged by Seasat (*2*). The long dimension of the putative Venusian dune field is roughly perpendicular to dome-related streaks on either side of the flow deposit; this relation implies that the dunes are of the transverse type. The streaks indicate that the wind flow was dominantly toward the west during streak formation, but a few streaks also extend to the east from domes. A test of whether our interpretation of a dune field is correct will be to image (during an extended mission) the area at various incidence angles. The speckle appearance should change because other dune facets would produce specular (that is, nadir) returns, and the area should become uniformly dark if the incidence angle becomes larger than the steepest slope.

Several dome-related streaks (Fig. 9) occur between 25° and 30° north latitude. In this area, the sediment supply is interpreted to be pyroclastic debris associated with volcanic deposits that mantle older plains (*21*). The inferred wind directions responsible for the dome-related streaks vary from southwest to south-southwest. When combined with the streak data from the Carson area, it is clear that surface wind flow on Venus is complex and has both zonal and meridional components and is modulated by topography.

Modification of volcanic and tectonic landforms provides evidence that a variety of other surficial processes are also at work on Venus. For example, in plains located just south of the equator, several volcanic flows

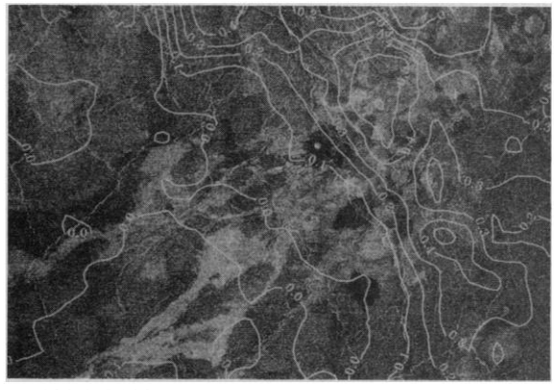

Fig. 10. Radar mosaic of equatorial plains region in Guinevere Planitia, with elevation contours in kilometers. Note the elongate regions of relatively high radar cross section that trend northeast-southwest. These are probably relatively young lava flows. The flows extend from a complex volcanic terrain with domical hills and regions of high and low backscatter. These units are interpreted to be superimposed on an older, bland fractured plains that has been modified by weathering, erosion, and deposition. Part of F-MIDR 05S335. Incidence angle is about 43°. Center latitude is −6.2°; center longitude is 341.4°; frame width is 145 km.

with relatively high radar cross sections are seen to cover a more muted, fractured plains (Fig. 10). Several younger flows with relatively low cross sections can also be discerned. It is likely that the superimposed flows are young enough to retain textures associated with their emplacement, accounting for the variable backscatter. Assume that the average crater retention age of 400 million years (*17, 18*) pertains to the fractured plains. Also assume that the flows that generated the fractured plains initially had variable radar cross sections. It then follows that over approximately 400 million years, surficial processes must have been sufficiently intense to remove distinct radar signatures associated with discrete flows that make up the fractured plains and to remove or subdue the topography associated with individual flows on these older plains. The extent of reworking corresponds approximately to removing or subduing height scales associated with blocks (centimeters to meters) and flow relief (meters). We note that cross sections for the fractured plains are typically 3 dB lower than the brighter, superimposed plains. These values are similar to cross-section differences found for old, subdued, as opposed to young basaltic flows at the Cima Volcanic Field (*12*).

If it is assumed that the upper limit (that is, meters) for the amount of reworking necessary to homogenize the fractured plains surface is correct, then the typical vertical resurfacing rate is similar to the rate computed on the basis of removal of the paraboloidal streaks. Alternatively, the reworking rate earlier in history may have been much higher, and a bland fractured plains was left that was later covered in some places with volcanic materials that have been preserved in pristine form. However, we favor the steady-state model in which surficial processes have operated continuously, albeit slowly, relative to resurfacing by volcanism and tectonism. Over short time scales, ejecta and other mobile material is redistributed by eolian processes, while over

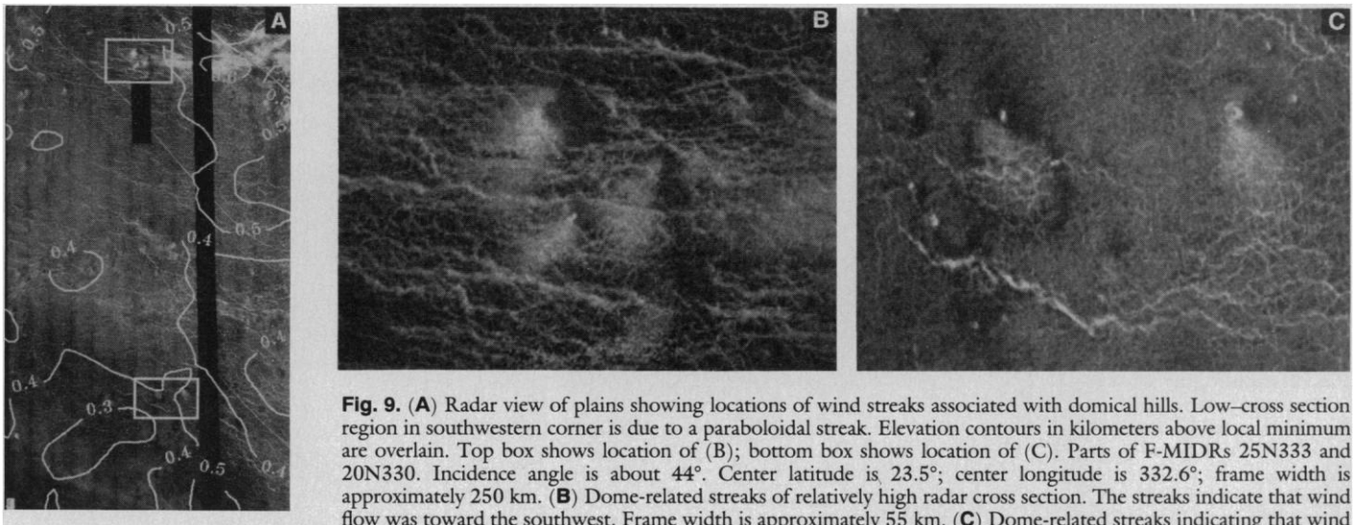

Fig. 9. (**A**) Radar view of plains showing locations of wind streaks associated with domical hills. Low–cross section region in southwestern corner is due to a paraboloidal streak. Elevation contours in kilometers above local minimum are overlain. Top box shows location of (B); bottom box shows location of (C). Parts of F-MIDRs 25N333 and 20N330. Incidence angle is about 44°. Center latitude is 23.5°; center longitude is 332.6°; frame width is approximately 250 km. (**B**) Dome-related streaks of relatively high radar cross section. The streaks indicate that wind flow was toward the southwest. Frame width is approximately 55 km. (**C**) Dome-related streaks indicating that wind flow was toward the south-southeast. Note that the perimeter of the large streak on the left has a relatively low cross sectionrelative to surroundings, consistent with accumulation of debris around the edge of an erosional core. Azimuthal spread in streaks is suggestive of a variable wind direction. Frame width is approximately 55 km.

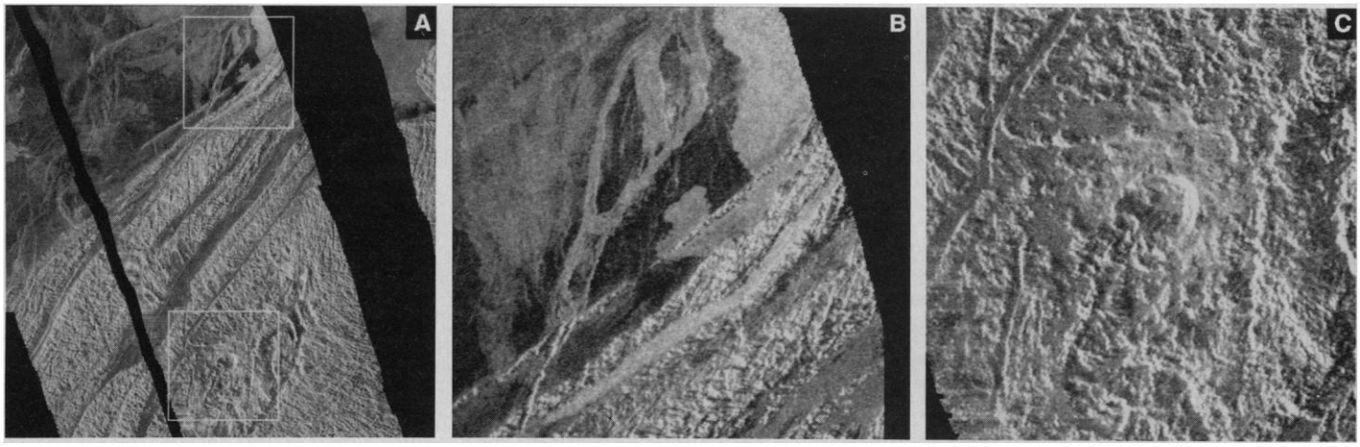

Fig. 11. (**A**) Tesserae and adjacent plains are shown for the northwest part of Lada Terra. Boxes show regions shown in (B) and (C). Part of C1-MIDR 65S005. Incidence angle is about 19°. Center latitude is −64.3°; center longitude is 12°; frame width is 290 km. (**B**) Enlargement of part of (A) showing channel that has cut through the tesserae and has eroded the plains material, leaving behind remnant islands. Frame width is 70 km. (**C**) Enlargement of part of (A) showing tesserae and impact crater with rim and ejecta deposits modified by tectonic activity and mass wasting. Frame width is 70 km.

longer time scales, plains surfaces are homogenized.

A high degree of erosion by lava is evident in several plains areas observed by Magellan. For example, in northwestern Lada Terra, plains have been disrupted by lavas flowing from south to north in the channel shown in Fig. 11, A and B; the flows led to extensive erosion and formation of remnant islands in the plains. A survey of Magellan data shows that a variety of channel forms are evident in the plains. Features include streamlined erosional remnants, ponding and overtopping of uplands, and complex anastomosing patterns.

Surface processes may be much more active in the uplifted, fractured tesserae than in the plains (Fig. 11). The tectonic processes that produce tesserae generate relief, disrupt bedrock at a variety of scales, and produce thick soil cover (*7, 8*). The relief and disrupted nature of the crust should lead to enhanced mass wasting. Direct evidence of mass wasting is found in a number of Magellan radar images covering the tesserae. The irregular contacts between tesserae upland blocks and plains also imply that considerable mass wasting has occurred. Combined with the atmosphere-surface interactions, the rate of resurfacing by surficial processes is thus probably greater in tesserae than in plains. These processes have probably contributed to the highly degraded nature of the impact crater shown in Fig. 11C as compared to the fresh appearance of plains craters (*17, 18*), although it appears that tectonic disruption may also have helped degrade this crater.

Finally, no surface features have been observed whose origin would require that Venus had a different climate during the past 400 million years. Unequivocal evidence of fluvial, lacustrine, or marine landforms and deposits has not been observed. Rather, we believe that processes similar to those that occur under the present ambient conditions have been quite capable of shaping the surface.

REFERENCES AND NOTES

1. V. L. Barsukov *et al.*, *Proc. Lunar Planet. Sci. Conf.* **17**, *J. Geophys. Res.* **91**, D378 (1986); J. W. Head and L. S. Crumpler, *Science* **238**, 1380 (1987); D. B. Campbell *et al.*, *ibid.* **246**, 373 (1989); R. E. Arvidson, J. J. Plaut, R. F. Jurgens, R. S. Saunders, M. A. Slade, *Proc. Lunar Planet Sci. Conf.* **20**, 557 (1990).
2. R. E. Arvidson *et al.*, *Icarus* **75**, 163 (1988).
3. R. S. Saunders *et al.*, *J. Geophys. Res.* **95**, 8339 (1990).
4. B. A. Ivanov, A. T. Basilevsky, V. P. Kryuchkov, I. M. Chernaya, *Proc. Lunar Planet. Sci. Conf.* **16**, *J. Geophys. Res.* **91**, D413 (1986); A. T. Basilevsky *et al.*, *J. Geophys. Res.* **92**, 12869 (1987).
5. B. Fegley and R. Prinn, *Nature* **337**, 55 (1989).
6. C. Sagan, *J. Atmos. Sci.* **32**, 1079 (1975); R. Greeley and R. E. Arvidson, *Earth Moon Planets* **50**, 127 (1990).
7. G. H. Pettengill, P. G. Ford, B. D. Chapman, *J. Geophys. Res.* **92**, 14881 (1988).
8. D. L. Bindschadler and J. W. Head, *Earth Moon Planet.* **42**, 133 (1988).
9. The Magellan Radar System collects several kinds of data. In the altimetric mode, the nadir-pointing horn antenna is used to record echo power as a function of time. These data are used to extract elevation beneath the spacecraft, along with estimates of Fresnel reflectivity and root-mean-square slopes at quasi-specular scattering length scales (that is, >12.6 cm). In the SAR mode, the high-gain antenna collects data to be used in generation of radar images. These products, shown in this paper as parts of mosaic image data records (MIDRs), have brightness values in proportion to normalized backscatter cross section, expressed in decibels. Between SAR bursts, the high-gain antenna is used in a passive mode to measure surface microwave emittance. The emittance is converted to emissivity values, which are shown in this paper. See G. H. Pettengill *et al.* [*Science* **252, 260** (1991)] for details of processing, and G. L. Tyler *et al.* (*ibid.*, p. 265), for an overview of the data and inferred surface properties.
10. We show emissivity as opposed to Fresnel reflectivity because emissivity is a more direct product to generate and because the data seem to suffer less from inter-orbit variations as compared to Fresnel reflectivity data. For a smooth surface, emissivity = 1 minus the Fresnel reflectivity, by Kirchoff's Law. Diffuse scale roughness affects emissivity. We quantify this affect over Danu Montes by using radar-cross-section values to remove the diffuse-scale roughness modulation of Fresnel reflectivities, as done in (7). Results demonstrate that Danu Montes still has a relatively high Fresnel reflectivity (0.3 to 0.4) and thus a low (0.6 to 0.7) emissivity. The control must be an enhanced dielectric constant.
11. R. S. Saunders, A. R. Dobrovolskis, R. Greeley, S. Wall, *Geophys. Res. Lett.* **17**, 1365 (1990).
12. Values were extracted from calibrated AIRSAR at C and L bands using HH polarization and an incidence angle of approximately 35°. Values quoted are average of C and L band cross section, weighted by the S-band wavelength of Magellan. Young flow quoted is known as I1; P3 is the old flow. From J. J. Plaut, thesis, Washington University, St. Louis (in preparation) using data acquired during the 1988 Mojave Field Experiment.
13. R. Greeley, P. Christensen, R. Carrasco, *Geology* **17**, 665 (1989).
14. G. Schubert, in *Venus*, D. M. Hunten *et al.*, Eds. (Univ. of Arizona Press, Tucson, AZ, 1983), pp. 681–69●.
15. G. S. Golitsyn, *Cosmic Res.* **16**, 156 (1978); C. C. Counselman III, S. A. Gourevitch, R. W. King, G. B. Loriot, E. S. Ginberg, *J. Geophys. Res.* **85**, 8026 (1980).
16. A. Dobrovolskis, *Icarus* **56**, 165 (1983).
17. R. J. Phillips *et al.*, *Science* **252**, 288 (1991).
18. R. E. Grimm and S. C. Solomon, *Geophys. Res. Lett.* **14**, 538 (1987); R. E. Arvidson, R. E. Grimm, R. J. Phillips, G. G. Schaber, E. M. Shoemaker, *ibid.* **17**, 1385 (1990).
19. Several craters have these flow-like ejecta deposits. See (*18*) for a more extensive discussion.
20. C. Elachi and R. Blom, *J. Geophys. Res.* **86**, 3061, (1981).
21. See J. W. Head *et al.* [*Science* **252, 276** (1991)] for more extensive discussion of evidence for pyroclastic volcanism.

22. We thank K. Chamberlain, R. Greeley, V. C. Gulick, K. B. Klose, G. Komatsu, T. Parker, S. Slavney, E. Stofan, and C. Weitz for help in preparing materials for this manuscript. We particularly thank J. J. Plaut for estimating the diffuse roughness effects on reflectivity. Supported by Jet Propulsion Laboratory contracts 957415 to R.E.A., 958497 to V.R.B., and 958593 to J.A.W.

15 January 1991; accepted 8 March 1991